Backstresses from dislocation interactions quantified by nanoindentation load-drop experiments

Christopher A. Thom[1], Lars N. Hansen[2], Thomas Breithaupt[1], David L. Goldsby[3], & Kathryn M. Kumamoto[1,2]

[1]Department of Earth Sciences, University of Oxford, Oxford, OX1 3AN, U.K.

[2]Department of Earth and Environmental Sciences, University of Minnesota-Twin Cities, Minneapolis, Minnesota, 55455, U.S.A.

[3]Department of Earth and Environmental Science, University of Pennsylvania, Philadelphia, Pennsylvania, 19104, U.S.A.

Key Points

- A nanoindentation load-drop method was developed to measure backstresses in materials with high dislocation densities at sub-micron length scales.
- The backstresses measured in three geologic materials agree with theoretical predictions of Taylor hardening.
- Backstresses result from long-range dislocation interactions, an athermal process that can occur over a range of deformation conditions.

Abstract

Recent work has identified the importance of strain hardening and backstresses among dislocations in the deformation of geologic materials at both high and low temperatures, but very few experimental measurements of such backstresses exist. Using a nanoindentation load-drop method and a self-similar

Berkovich tip, we measure backstresses in single crystals of olivine, quartz, and plagioclase feldspar at a range of indentation depths from 100–1750 nm, corresponding to densities of geometrically necessary dislocations (GND) of order 10^{14}–10^{15} m^{-2}. Our results reveal a power-law relationship between backstress and GND density with an exponent ranging from 0.44 to 0.55 for each material, in close agreement with the theoretical prediction (0.5) from Taylor hardening. This work provides experimental evidence of Taylor hardening in geologic materials and supports the assertion that backstress must be considered in both high- and low-temperature deformation.

Plain Language Summary

As a material is plastically deformed at room temperature, it often becomes stronger. In minerals, this strengthening is typically caused by the accumulation of linear defects within the material. These defects repel each other and push back with a strength predicted to be proportional to the square root of the defect density, but this relationship has not typically been observed for geologic materials. We developed a method to measure the strength of this pushback at very small scales for which the density of these defects in the crystal is high. Our results for three common geologic materials agree with predictions from theory and demonstrate that these defects must be considered when modeling deformation of rocks in Earth's interior.

1. Introduction

The transient rheology of the upper mantle is inferred to control the dynamics of many geologic phenomena, including post-seismic deformation (e.g., Freed et al., 2012; Wang et al., 2012; Hu et al., 2016; Qiu et al., 2018). Several studies have presented models to describe the transient rheological behavior following large earthquakes (e.g., Masuti et al., 2016; Moore et al., 2017; Muto et al., 2019), but the physical mechanism that gives rise to this complex time-dependent rheology is not well-constrained. For example, Masuti et al. (2016) used a strain hardening coefficient to modify an elastic stress element in their Burgers model, but noted that the functional form of the constitutive law was completely unknown.

Experiments on geologic materials have measured transient creep (e.g., Post, 1977; Durham et al., 1979; Gangi, 1983; Duval et al., 1983; Smith & Carpenter, 1987; Hanson & Spetzler, 1994; Chopra, 1997; Caswell et al., 2015; Hansen et al., 2020), but quantifying this rheological behavior using conventional creep experiments is challenging because it may be caused by the interplay of multiple deformation processes acting simultaneously. Examination of the microstructures in recent stress-reduction experiments on olivine single crystals by Hansen et al. (2020) suggested that time-dependent recoverable strain (i.e., anelasticity) at high temperatures arises due to a combination of dislocation glide and long-range elastic interactions among dislocations. These authors presented a microphysical model that arises naturally from the behavior of lattice dislocations and captures both transient and steady-state rheology over a wide range of conditions. Specifically, Hansen et al. (2020) suggested that geometrically necessary dislocations (GNDs), which are dislocations of the same sign needed to accommodate lattice curvature or gradients in local strain, are an important defect type controlling transient deformation at high temperature. These dislocations differ from statistically stored dislocations (SSDs) in that the lattice distortion of GNDs is not cancelled by dislocations of the opposite sign. Consequently, GNDs can exhibit long-range interactions over length scales of 1–100 microns (Wallis et al., 2017; 2020a; 2020b). These interactions ultimately lead to a backstress which opposes further deformation by dislocation glide, and the backstress measured in experiments can support 50+% of the applied stress (Hansen et al., 2020).

Recent work also identified backstresses at much higher total GND densities in olivine deformed by low-temperature plasticity (Hansen et al., 2019; Wallis et al., 2020a). In addition to identifying a length scale effect in the yield stress (effectively the Hall-Petch effect), Hansen et al. (2019) also demonstrated the presence of strain hardening and the Bauschinger effect, a well-known phenomenon in metallurgical literature wherein the yield stress of a material is reduced after the deformation direction is reversed (i.e., the yield stress in extension is reduced after initially yielding in compression, and vice versa). This phenomenon is commonly attributed to the effect of an internal backstress from GND interactions that acts in the opposite direction to the initial deformation (Dieter, 1986 Chapters 4.14, 6.16, and references therein). Using high-angular resolution electron backscatter diffraction (HR-EBSD), Wallis et al. (2020a) measured

the GND density of a deformed single crystal of olivine from Hansen et al. (2019) and demonstrated that the Bauschinger effect was indeed related to long-range elastic interactions among GNDs created during strain hardening. Wallis et al. (2020a) also identified similar microstructures beneath indents in olivine from Kumamoto et al. (2017), suggesting that the same physical mechanism (i.e., hardening due to dislocation interactions) occurs during nanoindentation. However, due to the significantly larger stresses in nanoindentation, the dislocation density was much higher than in samples deformed in Hansen et al. (2019).

In the present paper, we quantify the relationship between GND density and backstress in three common geologic materials (olivine, quartz, and plagioclase feldspar) using a novel nanoindentation method. Because nanoindentation localizes deformation in a small volume of material, the sample is essentially self-confined, and extremely high stresses can be applied without inducing fracture. Additionally, nanoindentation using a Berkovich (3-sided pyramid) tip offers a significant advantage in that it can be used to probe different microstructures (i.e., GND densities) at the same strain (~8% after Johnson, 1970) due to its self-similar geometry. We utilize this technique to demonstrate excellent quantitative agreement between our experiments and theoretical predictions of Taylor hardening (Taylor, 1934), which suggests that backstress should scale as the square root of GND density.

2. Methods

We have developed a method to measure the backstress from GNDs created during nanoindentation experiments. This method is similar to a stress-reduction test, a common technique used on macroscopic samples to measure anelasticity (e.g., Takeuchi & Argon, 1976; Blum & Weckert, 1987; Caswell et al., 2015; Hansen et al., 2020), with one key difference. Because the indentation stress is controlled by the mechanical response of the sample and not its physical dimensions, this type of experiment is more accurately described as a “load-drop” test. Only the applied load is prescribed in the experiment, and neither stress nor strain rate are controlled. Syed Asif and Pethica (1997) presented the only previous study that utilized load drops to measure changes in indentation creep behavior, but they did not quantify the backstress systematically in their study of tungsten and gallium arsenide single crystals.

Each of our experiments consisted of four parts: 1) an initial loading phase, 2) a short hold at constant load to measure indentation creep behavior, 3) a rapid load drop, and 4) another longer hold at a reduced constant load to measure the mechanical response of the sample. Segment 1 can be completed using any number of standard nanoindentation protocols, such as constant loading rate or constant nominal strain rate, as the main function of this step is to set the initial microstructure (i.e., GND density) beneath the indenter tip. The GND density, ρ_{GND}, below the indenter tip for a pyramidal geometry is a function of the tip shape, the indentation depth, *h*, and the Burgers vector, *b*, of the material (Nix & Gao, 1998; Pharr et al., 2010) and is given by

$$\rho_{\mathrm{GND}} = \frac{3\tan^2\theta}{2bh}, \qquad \text{(Eq. 1)}$$

where θ is the angle formed between the surface and the indenter (19.7° for a Berkovich tip). Thus, deeper indents formed by larger applied loads will result in a lower GND density. Previous work on soft metals has suggested that this approximation may overestimate the GND density when the radius of the hemisphere of the plastically deforming zone is larger than the indenter contact radius (e.g., Durst et al., 2005), but this geometric constraint remains valid for hard geologic materials such as olivine (see images in Wallis et al., 2020 for an example).

In the results presented here, all experiments were performed in a load-controlled nanoindentation apparatus with $\dot{P}/P$ = 0.2 for segment 1, where P is the applied load and $\dot{P}$ is its time derivative. The indentation hardness, *H*, is the mean contact stress, defined as

$$H = \frac{P}{A}, \qquad \text{(Eq. 2)}$$

where *A* is the projected contact area between the tip and the sample. The value of *A* is calibrated as a function of depth using a standard of known Young's modulus (usually fused silica) and given by the relationship

$$A = C_1 h_c^2 + C_2 h_c + C_3 h_c^{\frac{1}{2}} + ... + C_7 h_c^{\frac{1}{32}}, \qquad \text{(Eq. 3)}$$

where C_1, C_2, C_3...C_7 are constants, and h_c is the contact depth (i.e., the true depth at which the tip and sample are in contact, with elastic deflection of the surface of the sample removed). The contact depth is given by

$$h_c = h - \epsilon\frac{P}{S}, \quad \text{(Eq. 4)}$$

where h is the measured indentation depth, ϵ is a constant associated with the geometry of the indenter (0.75 for Berkovich), and S is the contact stiffness (Oliver & Pharr, 1992; 2004). With known contact stiffness and contact area, the reduced elastic modulus, E_r, of the tip-sample contact can be determined using

$$E_r = \frac{\sqrt{\pi}S}{2\sqrt{A}}. \quad \text{(Eq. 5)}$$

Utilizing known values of the elastic constants of the diamond tip and an assumed Poisson's ratio of the sample, we determined the sample's elastic modulus using

$$\frac{1}{E_r} = \frac{1-\nu_{\mathrm{s}}^2}{E_{\mathrm{s}}} + \frac{1-\nu_{\mathrm{i}}^2}{E_{\mathrm{i}}}, \quad \text{(Eq. 6)}$$

where E is the Young's modulus, ν is Poisson's ratio, and the subscripts s and i refer to the sample and indenter tip, respectively. Our experiments were performed using the continuous stiffness measurement (CSM) method with a dynamic frequency of 110 Hz and a target dynamic displacement of 2 nm, which allowed us to measure the contact stiffness (and therefore the contact depth, hardness, and elastic modulus of the sample) continuously as a function of time (Pethica & Oliver, 1988; Li & Bhushan, 2002; Oliver & Pharr, 2004).

Segment 2 of our load-drop method is optional, but in these experiments we performed a 60-s hold to measure the creep behavior and to allow the machine to settle. Due to possible thermal drift of the instrument, this portion of the test and all subsequent measurements were obtained using the CSM method. In this portion of the test, and all following steps, we used the measured elastic modulus from Segment 1 and rearrange Eq. 5 to solve for contact area as

$$A = \frac{\pi S^2}{4E_r^2}. \quad \text{(Eq. 7)}$$

This approach is preferable to relying on the depth measurement to acquire contact area using Eq. 3 and 4 because the depth measurement is highly sensitive to temperature fluctuations. Thus, our subsequent measurements of hardness from Eq. 2 are calculated from the measured contact stiffness, the previously derived elastic modulus, and the current applied load.

Segments 3 and 4 are the additions of our method and encompass a load drop and subsequent hold. In Segment 3 of our experiments, we reduced the load linearly over 1 s by a prescribed amount, ranging from 1% to 99% of the maximum applied load. A small amount of dynamic overshoot occurred for large reductions in applied load, but these variations did not significantly influence any of our results. After the load drop, the new applied load was held constant for the duration of Segment 4. In the results presented here, we held the load at the reduced value for 3600 s before completely unloading the sample.

In summary, this method determines the hardness and elastic modulus as a function of indentation depth and the creep behavior during a short hold at high stress. In addition, by testing a range of reductions in load for a given peak load, we can determine the magnitude of the backstress in a material, as demonstrated below. Repeating a series of experiments at different peak loads and thus different maximum depths, corresponding to different GND densities, also allows us to explore the influence of microstructure on backstress.

We performed a total of 155 load-drop experiments on single crystals of San Carlos olivine, synthetic quartz, and natural plagioclase feldspar (labradorite). The samples were polished with successively finer diamond suspensions down to 0.25 μm, then finished with a final step of 0.05 μm colloidal silica. For each experiment, we recorded the applied load, indentation depth, and contact stiffness at a rate of 100 Hz, from which we derived the elastic modulus, contact stress, and creep behavior at each point in the test.

3. Results

For each material, Segments 1 and 2 were reproducible for a given maximum load (e.g., Figure 1a), and the values obtained for the elastic modulus and scale-dependent hardness were consistent with previous

results on the same materials (Kumamoto et al., 2017; Thom et al., 2018). To discuss the results from Segments 3 and 4, we examine a representative set of experiments on olivine presented in Figure 1. In each experiment, the maximum applied load was 5 mN; thus the indentation depth (120 nm) and GND density (29.6×10^{14} m^{-2}) (Table 1) immediately prior to the load drops were approximately equivalent (Eq. 1). The only difference among these experiments was the magnitude of the load drop during Segment 3 of each test. Contact stiffness versus time for each experiment before and after the load drop are presented in Figure 1a, with each test segment labeled. An initial steep increase in contact stiffness occurs in Segment 1, and a small increase over time occurs in Segment 2. The abrupt reduction in contact stiffness occurs as the applied load is reduced in Segment 3 and is associated with some elastic recovery of the material.

In all experiments, one of three behaviors was observed after the load drop: 1) the contact stiffness increased with time (forward creep), 2) the contact stiffness decreased with time (backwards/reverse creep), or 3) there was no change in contact stiffness (negligible/no creep). In the examples in Figure 1a, one test demonstrates continued forward creep (1% load drop), three tests demonstrate backwards creep in the early portions of the hold (40%, 60%, and 90% load drops), and one test exhibits no change in the stiffness (30% load drop). The largest load drop where no creep occurred is taken to be the experiment where the contact stress is approximately equal to the backstress from dislocation interactions. Any larger load drops resulted in backwards creep.

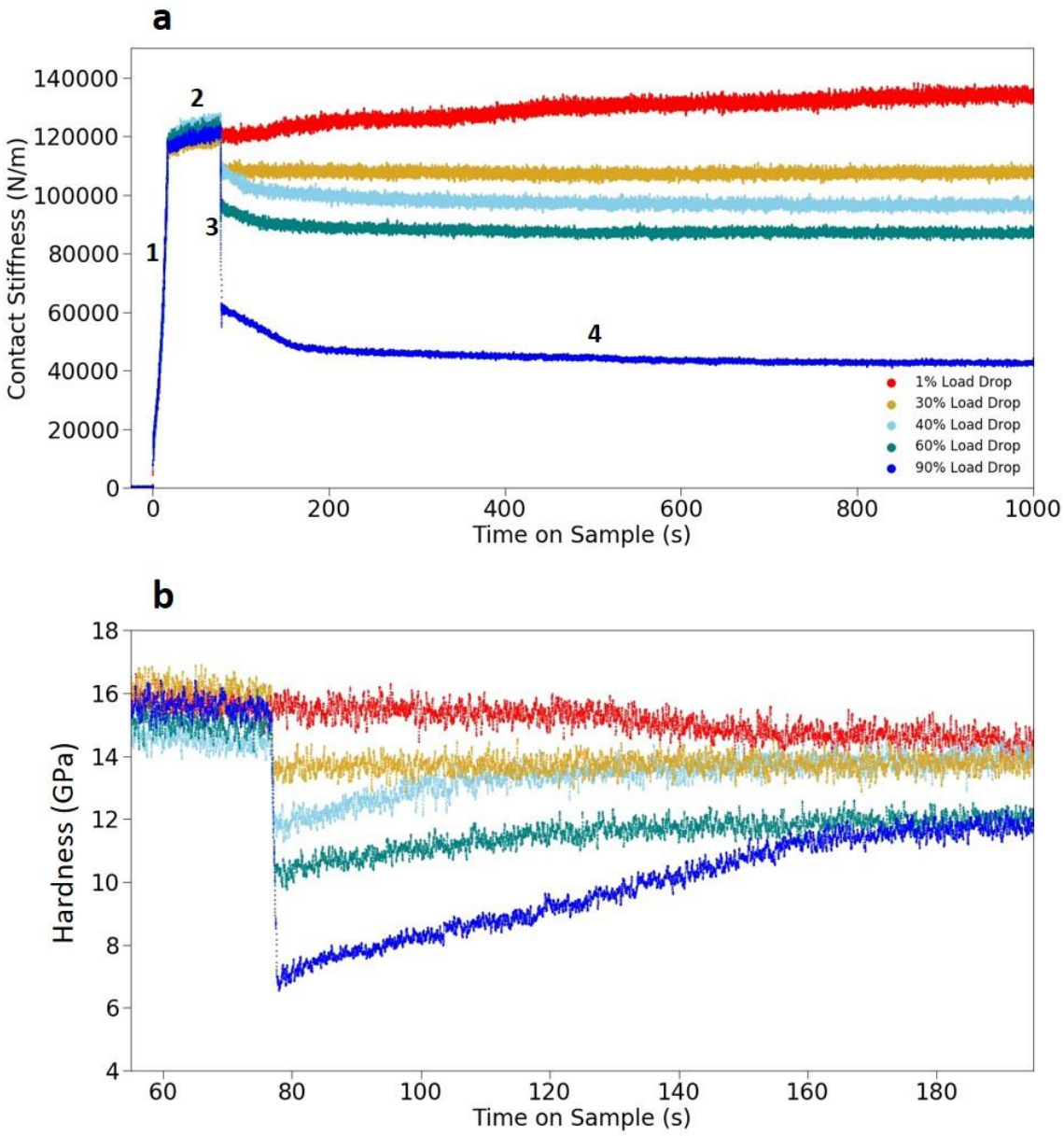

Figure 1: Contact stiffness (a) and hardness (b) vs. time on sample for five experiments on olivine at a peak load of 5 mN. The steep rise in stiffness at the beginning of the test in (a) represents Segment 1 of the experiment and the slow increase in stiffness over time in Segment 2 is due to creep (both labeled). Upon unloading by different percentages of the same peak load (Segment 3), both contact stiffness (a) and hardness (b) decrease due to some elastic recovery of the samples. During Segment 4, contact stiffness either continues to increase over time due to forward creep (e.g., for a 1% load drop), decreases due to reverse creep (e.g., for a 90% load drop), or remains constant over time (i.e., no creep as shown by the

194 *30% load drop). The corresponding response in hardness is shown in (b), where the hardness decreases*
195 *(forward creep), increases (backwards creep), or remains the same (no creep).*

196 We use the measured contact stiffness, the elastic modulus calculated from Segment 1, and Eq. 2
197 and 7 to determine the hardness in the experiments in Figure 1a. These data are presented in Figure 1b for
198 a portion of the experiments shortly before and after the load drop. For a load drop of 1%, hardness
199 decreases slightly over time due to forward creep, consistent with previous nanoindentation creep
200 experiments on geologic materials (e.g., Thom & Goldsby, 2019). Tests in which the backstress exceeds
201 the applied stress result in an increase in the measured hardness over time after the load drop (40%, 60%,
202 and 90% load drops), and the experiment with no creep (30% load drop) shows constant hardness with
203 time. The hardness for the experiment with the 30% load drop in Figure 1b is 13.8 GPa, which we infer to
204 be the backstress associated with the GND density in these experiments.

205 By varying the maximum applied load and thereby reaching different initial indentation depths, we
206 are able to probe the backstress of each material over GND densities varying by approximately one order
207 of magnitude. A summary of the data used to construct Figure 2a is presented in Table 1. Each data point
208 is derived from a series of experiments like those in Figure 1. For each material, a best-fit line is marked
209 by the solid line of the respective color, with power-law exponents of 0.44, 0.55, and 0.46 for olivine,
210 quartz, and feldspar, respectively. The average exponent across the materials is 0.49. In addition, a dashed
211 line of the same color is forced through the data with a slope of 0.5, representing the theoretical fit from the
212 hardening component of the Taylor equation (Taylor, 1934), which is given by

213 $$\sigma_b = \alpha G b \sqrt{\rho}_{\mathrm{GND}}, \qquad \text{(Eq. 8)}$$

214 where σ_b is the backstress associated with hardening from GNDs, α is a constant, G is the shear modulus,
215 and b is the Burgers vector. For each material, the data are adequately fit by the dashed lines, but because
216 the data only span one order of magnitude in GND density, it is difficult to evaluate the robustness of the
217 fits, similar to previous assessments of the Hall-Petch effect (Dunstan & Bushby, 2014; Li et al., 2016). A
218 non-dimensional plot of the backstress normalized by the Young's modulus derived from the indentation
219 tests and the GND density normalized by the Burgers vector squared of the material reveals remarkable

data collapse, as shown in Figure 2b. A solid black line represents the best fit to all normalized data with a slope of 0.47, and a dashed black line is presented with a slope of 0.5 for comparison to the theoretical prediction. This data collapse suggests that the value of α in the Taylor equation is the same for all materials tested here. Because we are measuring the axial backstress and Young's modulus, some assumptions related to Poisson's ratio are needed to quantify the value of α as presented in shear in Eq. 8. A value α = 3.6 +/- 0.1 best fits the data, but assuming a value of 0 for Poisson's ratio results in α = 2.7. In either case, this value is broadly consistent with experimental observations in metals (e.g., Lavrentev, 1980 and references therein) and is not the specific focus of this manuscript.

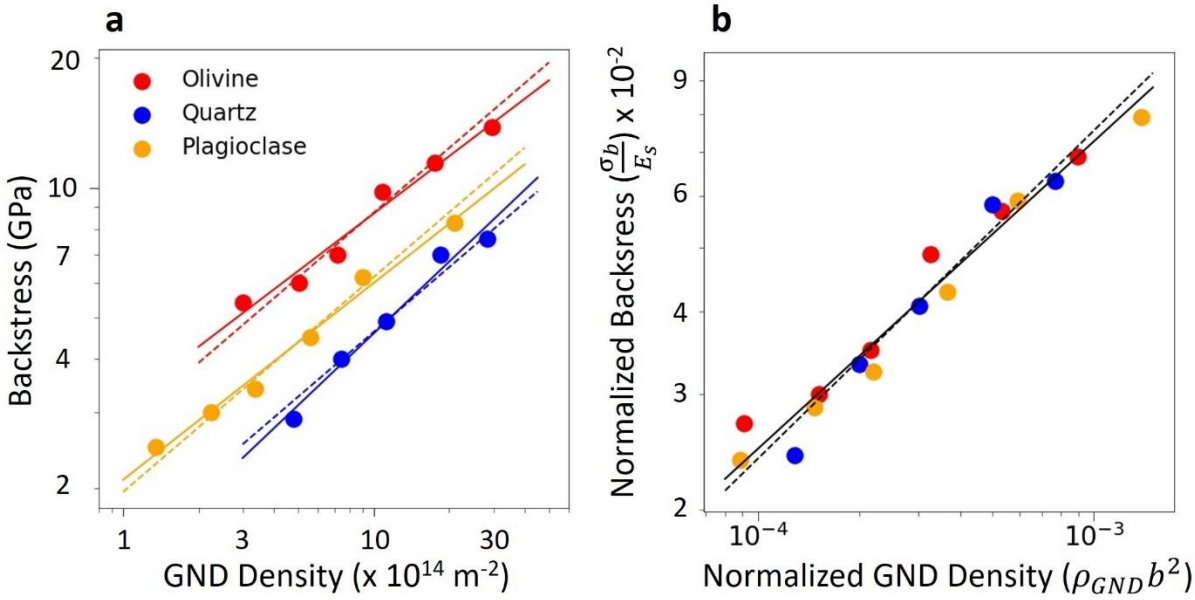

Figure 2: Results of all experiments on olivine, quartz, and plagioclase feldspar demonstrating that backstress (a) and normalized backstress (b) are a function of the initial (normalized) microstructure, or (normalized) GND density. Each data point in (a) and (b) is found using a series of experiments like those depicted in Figure 1. The solid lines in (a) are best fits to each individual set of data (slope of 0.44 for olivine, 0.55 for quartz, and 0.46 for plagioclase feldspar, with an average value of 0.49), and each dotted line is the forced fit of a line with a slope of 0.5, which is predicted from the Taylor hardening equation. In (b), the backstress is normalized by the Young's modulus derived from Segment 1 of the indentation test (200 GPa for olivine, 120 GPa for quartz, and 105 GPa for plagioclase feldspar) and the appropriate

Burgers vector (0.55, 0.52, and 0.81 nm, respectively). The solid black line is a best fit to all the normalized data with a slope of 0.47, and the dashed black line is a forced fit to the data with a slope of 0.5.

Table 1: Target maximum applied load, average maximum indentation depth, backstress, and GND density for all data presented in Figure 2a.

Sample	Maximum Load (mN)	Indentation Depth (nm)	Backstress (GPa)	GND Density (x 10^{14} m^{-2})
Olivine	5	120	13.8	29.6
	15	200	11.4	17.6
	25	320	9.8	10.8
	65	480	7.0	7.2
	100	690	6.0	5.0
	300	1150	5.4	3.0
Quartz	5	130	7.6	28.4
	10	200	7.0	18.5
	25	330	4.9	11.2
	50	500	4.0	7.4
	100	780	2.9	4.8
Plag	2	110	8.3	21.1
	10	260	6.2	9.1
	25	420	4.5	5.6
	70	700	3.4	3.4
	150	1050	3.0	2.2
	400	1750	2.5	1.4

4. Discussion

We compare our olivine data to other measurements of backstress and GND density in single crystals of olivine in Figure 3. Data from this study are shown in red at high GND density, data from a

room-temperature deformation-DIA (D-DIA) experiment of Hansen et al. (2019) are shown in blue at intermediate GND density, and data from the high-temperature (1523-1573 K) experiments of Hansen et al. (2020) are shown in black at the lowest GND density. The solid black data point represents a sample where the GND density was directly measured, and the open black circles represent GND densities inferred by using the dislocation density piezometer of Bai & Kohlstedt (1991) and assuming all dislocations are GNDs. We note that the inferred GND density of the sample with a direct measurement is within the error bars, suggesting our assumption of all dislocations being GNDs is reasonable. We also reiterate the distinction between backstress and applied stress, as these two values are not equivalent. Only backstresses directly measured in experiments are plotted in Figure 3. The dashed red line presented in Figure 3 is the same as in Figure 2a (it is only fit to the nanoindentation data), while the black dashed line is a forced fit of the Taylor equation to the high-temperature data. The room-temperature experiment of Hansen et al. (2019) falls on the same line as the indentation data presented here, while the high-temperature data appear to be systematically offset to lower backstresses (i.e., with a smaller value of α).

While we do not observe a universal relationship between high- and low-temperature experiments, these results are consistent with the microphysical model presented by Hansen et al. (2020), in which transient and steady-state rheology are captured by a combination of dislocation glide and elastic interactions among GNDs. The value of α may be temperature-dependent or a function of the differential stress, but more experiments at intermediate conditions are needed to resolve this subtlety. However, this study provides direct evidence of Taylor hardening in geologic materials at room temperature, and future work will explicitly link the Taylor equation (i.e., the evolution of backstress with GND density) to transient rheology over a wide range of conditions. The presence of Taylor hardening in all minerals tested here and the remarkable data collapse presented in Fig. 2b suggests that transient deformation of other geologic materials may be parameterized in a similar manner to that in Hansen et al. (2019; 2020), and that microstructural evolution models must incorporate the Taylor relationship.

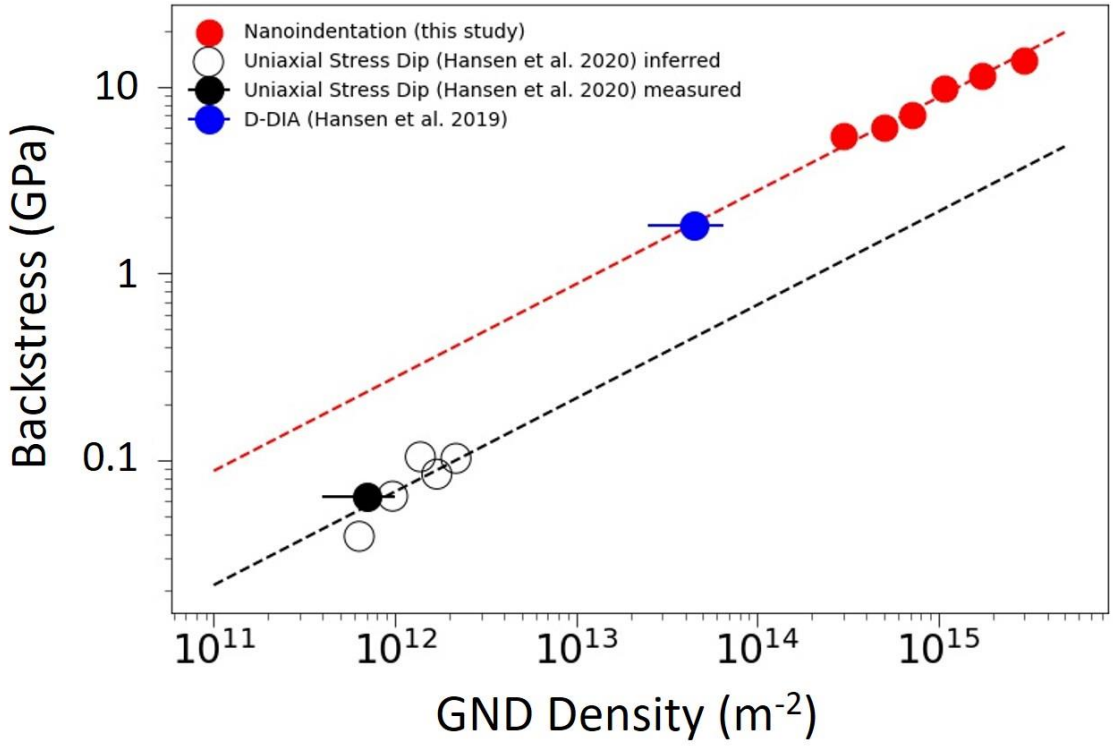

Figure 3: Compilation of backstress and GND density data from studies of single crystals of San Carlos olivine which measure both values. Results from room temperature indentation tests (this study) are shown in red, the room temperature D-DIA experiment from Hansen et al. (2019) analyzed by Wallis et al. (2020a) is shown in blue, and the high temperature stress dip experiments from Hansen et al. (2020) are shown in black (the direct GND measurement is represented by the solid circle, while inferred GND values are represented by the open circles). Horizontal error bars reflect uncertainty in the average GND density determined via HR-EBSD. The dashed red and black lines are fits of the Taylor hardening equation for the nanoindentation and high-temperature stress dips, respectively.

5. Conclusions

We have performed nanoindentation load-drop experiments on single crystals of olivine, quartz, and plagioclase feldspar to measure the backstress created by long-range elastic interactions among dislocations. To vary the GND density, we applied a range of maximum loads using a self-similar

Berkovich indenter tip to achieve a range of indentation depths. Our results demonstrate that the backstress in all three materials scales approximately with the square root of GND density, as predicted from the Taylor hardening equation. The value of α in the Taylor equation is similar among all materials tested here at room temperature but varies from that inferred in high-temperature experiments, suggesting that recovery or stress may play a role in modifying the backstress. However, these results are consistent with the microphysical model presented by Hansen et al. (2020), which suggests that backstress and its evolution are important physical processes that must be considered in studies of deforming geologic materials, including during transient deformation at both high- and low-temperature.

Acknowledgements

C.A.T. designed the study and nanoindentation method, carried out experiments and data analysis, and wrote the initial manuscript draft. All authors contributed to editing and revising the manuscript. The authors would like to thank G. Pharr and D. Wallis for useful discussions. All data used in this study are available at https://upenn.box.com/s/mo9txpz9n6dzvdup6dt5yq8t6ltd80tt. Funding for this study was provided by NERC 1710DG008/JC4 to L.N.H. and C.A.T. and NSF EAR-1806791 to K.M.K.

References

1. Bai, Q., Mackewll, S.J., & Kohlstedt, D.L. (1991). High-temperature creep of olivine single crystals 1. Mechanical results for buffered samples. *Journal of Geophysical Research, 96*(B2), 2241-2463. https://doi.org/10.1029/90JB01723
2. Blum, W., & Weckert, E. (1987). On the interpretation of the “internal stress” determined from dip tests during creep of Al-5at.%Mg. *Materials Science and Engineering*, *86*, 145-158. https://doi.org/10.1016/0025-5416(87)90449-6
3. Caswell, T.E., Cooper, R.F., & Goldsby, D.L. (2015). The constant-hardness creep compliance of polycrystalline ice. *Geophysical Research Letters*, *42*(15), 6261-6268. https://doi.org/10.1002/2015GL064666

4. Chopra, P.N. (1997). High-temperature transient creep in olivine rocks. *Tectonophysics*, *279*(1-4), 93-111. https://doi.org/10.1016/S0040-1951(97)00134-0
5. Dieter, G.E. (1986). *Mechanical Metallurgy*. New York, NY: McGraw-Hill Education.
6. Dunstan, D.J., & Bushby, A.J. (2014). Grain size dependence of the strength of metals: The Hall–Petch effect does not scale as the inverse square root of grain size. *International Journal of Plasticity*, *53*, 56-65. https://doi.org/10.1016/j.ijplas.2013.07.004
7. Durham, W.B., Froidevaux, C., & Jaoul, O. (1979). Transient and steady-state creep of pure forsterite at low stress. *Physics of the Earth and Planetary Interiors*, *19*(3), 263-274. https://doi.org/10.1016/0031-9201(79)90027-X
8. Durst, K., Backes, B., & Goken, M. (2005). Indentation size effect in metallic materials: Correcting for the size of the plastic zone. *Scripta Materialia*, *52*, 1093-1097. https://doi.org/10.1016/j.scriptamat.2005.02.009
9. Duval, P., Ashby, M.F., & Anderman, I. (1983). Rate-controlling processes in the creep of polycrystalline ice. *Journal of Physical Chemistry*, *87*(21), 4066-4074. https://doi.org/10.1021/j100244a014
10. Freed, A.M., Hirth, G., & Behn, M.D. (2012). Using short-term postseismic displacements to infer the ambient deformation conditions of the upper mantle. *Journal of Geophysical Research*, *117*(B1), B01409. https://doi.org/10.1029/2011JB008562
11. Gangi, A.F. (1983). Transient and steady-state deformation of synthetic rocksalt. *Tectonophysics*, *91*(1-2), 137-156. https://doi.org/10.1016/0040-1951(83)90062-8
12. Hansen, L.N., Kumamoto, K.M., Thom, C.A., Wallis, D., Durham, W.B., Goldsby, D.L., et al. (2019). Low-temperature plasticity in olivine: Grain size, strain hardening, and the strength of the lithosphere. *Journal of Geophysical Research*, *124*(6), 5427-5449. https://doi.org/10.1029/2018JB016736

13. Hansen, L.N., Wallis, D., Breithaupt, T., Thom, C.A., & Kempton, I. (2020). Dislocation creep of olivine: Low-temperature plasticity controls transient creep at high temperatures. https://doi.org/10.1002/essoar.10504736.1
14. Hanson, D.R., & Spetzler, H.A. (1994). Transient creep in natural and synthetic, iron-bearing olivine single crystals: Mechanical results and dislocation microstructures. *Tectonophysics*, *235*(4), 293-315. https://doi.org/10.1016/0040-1951(94)90191-0
15. Hu, Y., Bürgmann, R., Uchida, N., Banerjee, P., & Freymueller, J.T. (2016). Stress-driven relaxation of heterogeneous upper mantle and time-dependent afterslip following the 2011 Tohoku earthquake. *Journal of Geophysical Research: Solid Earth*, *121*(1), 385-411. https://doi.org/10.1002/2015JB012508
16. Johnson, K.L. (1970). The correlation of indentation experiments. *Journal of the Mechanics and Physics of Solids*, *18*(2), 115-126. https://doi.org/10.1016/0022-5096(70)90029-3
17. Kumamoto, K.M., Thom, C.A., Wallis, D., Hansen, L.N., Armstrong, D.E.J., Warren, J.M., et al. (2017). Size effects resolve discrepancies in 40 years of work on low-temperature plasticity in olivine. *Science Advances*, *3*(9), e1701338. https://doi.org/10.1126/sciadv.1701338
18. Lavrentev, F.F. (1980). The type of dislocation interaction as the factor determining work hardening. *Materials Science and Engineering*, *46*, 191-208. https://doi.org/10.1016/0025-5416(80)90175-5
19. Li, X., & Bhushan, B. (2002). A review of nanoindentation continuous stiffness measurement technique and its application. *Materials Characterization*, *48*(1), 11-36. https://doi.org/10.1016/S1044-5803(02)00192-4
20. Li, Y., Bushby, A.J., & Dunstan, D.J. (2016). The Hall-Petch effect as a manifestation of the general size effect. *Proceedings of the Royal Society A*, *472*. https://doi.org/10.1098/rspa.2015.0890

21. Masuti, S., Barbot, S., Karato, S.-I., Feng, L., & Banerjee, P. (2016). Upper-mantle water stratification inferred from observations of the 2012 Indian Ocean earthquake. *Nature*, *538*, 373-377. https://doi.org/10.1038/nature19783
22. Moore, J.D.P., Yu, H., Tang, C-H., Wang, T., Barbot, S., Peng, D., et al. (2017). Imaging the distribution of transient viscosity after the 2016 M_w 7.1 Kumamoto earthquake. *Science*, *356*(6334), 163-167. https://doi.org/10.1126/science.aal3422
23. Muto, J., Moore, J.D.P., Barbot, S., Iinuma, T., Ohta, Y., & Iwamori, H. (2019). Coupled afterslip and transient mantle flow after the 2011 Tohoku earthquake. *Science Advances*, *5*(9), eaaw1164. https://doi.org/10.1126/sciadv.aaw1164
24. Nix, W.D., & Gao, H. (1998). Indentation size effects in crystalline materials: A law for strain gradient plasticity. *Journal of the Mechanics and Physics of Solids*, *46*(3), 411-425. https://doi.org/10.1016/S0022-5096(97)00086-0
25. Oliver, W.C., & Pharr, G.M. (1992). An improved technique for determining hardness and elastic modulus using load and displacement sensing indentation experiments. *Journal of Materials Research*, *7*(6), 1564-1583. https://doi.org/10.1557/JMR.1992.1564
26. Oliver, W.C., & Pharr, G.M. (2004). Measurement of hardness and elastic modulus by instrumented indentation: Advances in understanding and refinements to methodology. *Journal of Materials Research*, *19*(1), 3-20. https://doi.org/10.1557/jmr.2004.19.1.3
27. Pethica, J.B., & Oliver, W.C. (1988). Mechanical properties of nanometre volumes of material: Use of the elastic response of small area indentations. *MRS Online Proceedings Library*, *130*, 13-23. https://doi.org/10.1557/PROC-130-13
28. Pharr, G.M., Herbert, E.G., & Gao, Y. (2010). The indentation size effect: A critical examination of experimental observations and mechanistic interpretations. *Annual Review of Materials Research*, *40*, 271-292. https://doi.org/10.1146/annurev-matsci-070909-104456
29. Post, R.L. (1977). High-temperature creep of Mt. Burnet dunite. *Tectonophysics*, *42*(2-4), 75-110. https://doi.org/10.1016/0040-1951(77)90162-7

30. Qiu, Q., Moore, J.D.P., Barbot, S., Feng, L., & Hill, E.M. (2018). Transient rheology of the Sumatran mantle wedge revealed by a decade of great earthquakes. *Nature Communications*, *9*, 995. https://doi.org/10.1038/s41467-018-03298-6
31. Smith, B.K., & Carpenter, F.O. (1987). Transient creep in orthosilicates. *Physics of Earth and Planetary Interiors*, *49*(3-4), 314-324. https://doi.org/10.1016/0031-9201(87)90033-1
32. Syed Asif, S.A. & Pethica, J.B. (1997). Nanoindentation creep of single-crystal tungsten and gallium arsenide. *Philosophical Magazine A*, *76*(6), 1105-1118. https://doi.org/10.1080/01418619708214217
33. Taylor, G.I. (1934). The mechanism of plastic deformation of crystals. Part I.- Theoretical. *Proceedings of the Royal Society A*, *145*(855). https://doi.org/10.1098/rspa.1934.0106
34. Takeuchi, S., & Argon, A.S. (1976). Steady-state creep of single-phase crystalline matter at high temperature. *Journal of Materials Science*, *11*, 1542-1566. https://doi.org/10.1007/BF00540888
35. Thom, C.A., Carpick, R.W., & Goldsby, D.L. (2018). Constraints on the physical mechanism of frictional aging from nanoindentation. *Geophysical Research Letters*, *45*(24), 13,306-13,311. https://doi.org/10.1029/2018GL080561
36. Thom, C.A., & Goldsby, D.L. (2019). Nanoindentation studies of plasticity and dislocation creep in halite. *Geosciences*, *9*(2), 79. https://doi.org/10.3390/geosciences9020079
37. Wallis, D., Hansen, L.N., Britton, T.B., & Wilkinson, A.J. (2017). Dislocation interactions in olivine revealed by HR-EBSD. *Journal of Geophysical Research: Solid Earth*, *122*, 7659-7678. https://doi.org/10.1002/2017JB014513
38. Wallis, D., Hansen, L.N., Kumamoto, K.M., Thom, C.A., Plümper, O., Ohl, M., et al. (2020a). Dislocation interactions during low-temperature plasticity of olivine and their impact on the evolution of lithospheric strength. *Earth and Planetary Science Letters*, *543*, 116349. https://doi.org/10.1016/j.epsl.2020.116349
39. Wallis, D., Hansen, L.N., Wilkinson, A.J., & Lebensohn, R.A. (2020b). Dislocation interactions in olivine control postseismic creep of the upper mantle. arXiv:2006.05195

40. Wang, L., Shum, C.K., Simons, F.J., Tapley, B., & Dai, C. (2012). Coseismic and postseismic deformation of the 2011 Tohoku-Oki earthquake constrained by GRACE gravimetry. *Geophysical Research Letters*, *39*(7), L07301. https://doi.org/10.1029/2012GL051104